





# A targeted and synergetic nano-delivery system against *Pseudomonas aeruginosa* infection for promoting wound healing

Chang Ni<sup>1</sup> , Xisheng Li<sup>1</sup>, Haiye Jiang, Shumin Gui, Heng Yin, Xinmin Nie<sup>\*</sup> 

Department of Laboratory Medicine, The Third Xiangya Hospital, Central South University, Changsha, 410013, Hunan Province, China

## ARTICLE INFO

### Keywords:

Pretreated macrophage membrane  
Nano drug delivery system  
Curcumin  
Ceftazidime  
*Pseudomonas aeruginosa*  
Wound healing

## ABSTRACT

**Purpose:** *Pseudomonas aeruginosa* infection is the most common pathogen in burn wound infections, causing delayed wound healing and progression to chronic wounds. Therefore, there is an urgent need to develop antimicrobial agents that can promote wound healing for effectively treating infected wounds.

**Patients and methods:** Using magnetic stirring and ultrasound to synthesize Apt-pM@UCNPmSiO<sub>2</sub>-Cur-CAZ. The nanosystems were characterized using transmission electron microscopy (TEM), dynamic light scattering (DLS), and ultraviolet-visible spectrophotometry (UV-Vis). Flow cytometry, bacterial LIVE/DEAD staining and scanning electron microscopy were performed to assess the in vitro antibacterial and anti-biofilm effects of the nanosystems. The wound healing potential and in vivo toxicity of the nanosystems were evaluated in a mouse skin wound model.

**Results:** The Apt-pM@UCNPmSiO<sub>2</sub>-Cur-CAZ synthesized exhibited uniform circular shape with a Zeta potential of -0.8 mV. In vitro, Apt-pM@UCNPmSiO<sub>2</sub>-Cur-CAZ demonstrated superior antibacterial effects compared to standalone antibiotics. Bacteria treated with Apt-pM@UCNPmSiO<sub>2</sub>-Cur-CAZ showed varying degrees of deformation and shrinkage, resulting in severe damage to the bacterial cells. Additionally, Apt-pM@UCNPmSiO<sub>2</sub>-Cur-CAZ can inhibit and eradicate bacterial biofilms, while also targeting bacteria for enhanced antibacterial efficacy. Interestingly, the NIR light could enhance the antibacterial and anti-biofilm effects of Apt-pM@UCNPmSiO<sub>2</sub>-Cur-CAZ due to the photodynamic action. In a mouse skin wound infection model, the nanosystem effectively eliminated wound bacteria, promoting the healing of *Pseudomonas aeruginosa*-infected wounds without significant toxic effects.

**Conclusion:** Apt-pM@UCNPmSiO<sub>2</sub>-Cur-CAZ is a novel targeted nano-delivery system with promising potential in combating *Pseudomonas aeruginosa* infections, and it may serve as a new therapeutic approach for treating skin wound infections.

## 1. Introduction

The skin is the body's largest and most exterior organ, making it susceptible to various factors such as physical trauma, chemical exposure, and pathogen invasion [1]. These factors can disrupt the normal structure of skin tissue and lead to wound formation. The process of wound repair is complex and involves four consecutive and coordinated stages: hemostasis, inflammation, proliferation, and remodeling [2]. Various factors can influence wound healing at each stage, such as excessive inflammation, burns, and infections [3,4]. Bacterial infection is a significant hindrance to wound healing due to excessive inflammation that can disrupt remaining epithelial tissue, leading to collagen

metabolism disorders, wound breakdown, and even damage to surrounding healthy tissue, resulting in chronic wounds [5]. This not only affects the patient's quality of life, but also increases morbidity and mortality rates, posing a significant threat to global public health [6].

*Pseudomonas aeruginosa* (*P. aeruginosa*), as one of the most common pathogens causing wound infections, is widely present in various environments and is a conditionally pathogenic bacterium [7]. The bacterium is characterized by easy colonization, phenotypic variation, and multidrug resistance, making it a major pathogen in hospital-acquired infections [8,9]. Due to its high resistance rate and limited effective antimicrobial agents, the treatment of *P. aeruginosa* infections is challenging [10]. As its resistance becomes increasingly serious,

\* Corresponding author.

E-mail address: [niixinmin@csu.edu.cn](mailto:niixinmin@csu.edu.cn) (X. Nie).

<sup>1</sup> These authors contributed equally to this work.

*P. aeruginosa* has become one of the difficult-to-treat ESKAPE (*Enterococcus faecium*, *Staphylococcus aureus*, *Klebsiella pneumoniae*, *Acinetobacter baumannii*, *P. aeruginosa*, and *Enterobacter species*) pathogens [11]. *P. aeruginosa* infection can cause severe inflammation, which can lead to unhealed skin damage resulting in a chronic wound [12]. The bacterium typically adheres to the skin's epithelial surface and forms biofilms [13, 14]. The biofilm creates a physical barrier that hinders the clearance of bacteria by antimicrobial drugs and significantly impairs the wound healing process [15,16]. Although recent drugs and dressings have shown efficacy in promoting wound healing, most lack strong antimicrobial and anti-biofilm capabilities to effectively treat infected wounds [17]. Therefore, there is an urgent need to develop new treatment approaches for infected skin wounds.

Antimicrobial photodynamic therapy (aPDT) is a strategy to achieve antimicrobial effects without the use of antibiotics [18,19]. It not only can kill microorganisms at the infection site but also promote wound healing at the site of infection [20]. Upconversion nanoparticles (UCNPs) are a novel fluorescent material that can absorb near-infrared (NIR) light, emit ultraviolet or visible light, and activate photosensitizers (PS) for antimicrobial purposes [21,22]. However, the use of UCNPs in the biological field is limited, requiring surface modifications to provide additional functionalities. Among the various surface modification strategies, mesoporous silica nanoparticles (MSNs) exhibit unique advantages such as tunable pore size and good biocompatibility, making them widely used as drug carriers [23,24]. Nanoparticle-based drug delivery systems are a new approach to improve drug solubility, bioavailability and reduction of drug side effects [25,26]. They can enhance drug permeability and also increase the susceptibility of bacteria to antibiotics, thereby improving treatment efficacy [27]. Additionally, recent studies have shown that curcumin (Cur), a low-toxic photosensitizer, possesses antimicrobial, anti-inflammatory, and antioxidant properties [28,29]. Therefore, curcumin can be loaded on UCNPs to generate aPDT under NIR light for the treatment of wounds infected with *P. aeruginosa*.

While artificial synthesis of nanoparticles has demonstrated exceptional antibacterial performance, these nanoparticles often exhibit toxicity, immunogenicity and lack of targeting capabilities, hindering their clinical application [30]. Recently, utilizing natural cell membrane coating for nanoparticles has emerged as a novel approach due to its ability to provide advantages such as prolonged circulation, active targeting, and high biocompatibility [31–34]. Macrophages are the primary cells that respond to pathogens in the body, serving as both sentinels and the first line of defense against bacterial infections [35]. Macrophages recognize various foreign microorganisms through pattern recognition receptors (PRRs) expressed on their surface, such as Toll-like receptors (TLRs) [36–38]. They swiftly respond to endogenous stimuli generated post-infection or signals from immune cells [39]. Studies have indicated that precise targeting of bacteria can be achieved by coating nanoparticles with macrophage membranes pre-treated with lipopolysaccharides (LPS) on the nanoparticle surface to enhance therapeutic efficacy [40]. Aptamers are short, single-stranded DNA or RNA oligonucleotides [41]. They are small molecules that are relatively non-immunogenic and easily chemically modified [42]. F23 is an aptamer that binds specifically to *Pseudomonas aeruginosa* and studies have demonstrated its sensitivity and specificity in the detection of this bacterium [43,44].

This study utilized mesoporous silica-coated UCNPs (UCNPmSiO<sub>2</sub>) as a drug delivery carrier for efficient loading of Cur and ceftazidime (CAZ). Pre-treated macrophage membranes (pM) were modified with F23 aptamer to synthesize a dual-targeting functional cell membrane. The synthesized Apt-pM encapsulated UCNPMSiO<sub>2</sub>-Cur-CAZ to form a novel biomimetic antibacterial nano-system, Apt-pM@UCNPmSiO<sub>2</sub>-Cur-CAZ. The system exhibited a remarkable ability to load drugs, high biocompatibility, photodynamic therapy, and superior antibacterial performance. Furthermore, it improved bacterial sensitivity to CAZ, effectively and rapidly targeting and eliminating bacteria. This presents

a new and efficient approach to treating *P. aeruginosa* infections in skin wounds.

## 2. Material and methods

### 2.1. Materials

Mesoporous silica coated upconverting nanoparticles (Purple blue light) were purchased from Xi'an Ruixi Biological Technology Co., Ltd. (China). Fetal bovine serum (FBS), penicillin–streptomycin cocktail, high glucose (Dulbecco's modified Eagle's medium-DMEM) and trypsin were obtained from Procell (China). Ceftazidime, Luria–Bertani (LB), Mueller–Hinton (MH), hematoxylin and eosin (HE) were provided by Solarbio Technology (China). Cell Counting Kit-8 (CCK-8) and Annexin V-FITC/PI apoptosis kit were purchased from ApexBio Technology (China). Curcumin was purchased from Chengdu Desite Biological Technology Co., Ltd (Chengdu, China). The aptamer sequence F23 (5'-CCCCCGTTGCTTTCGCTTTTCTTTCGCTTTTGTTCGTTTCGTCCCTGCTTCTTTCTTG-3') was obtained from Sangon Biotech (China). Lipopolysaccharides was provided by Sigma–Aldrich (USA). PE-conjugated anti-CD284 and PE-conjugated anti-CD14 antibodies were purchased from Biolegend (USA). The bacterial freezing medium, coomassie blue fast staining solution, crystal violet (CV) and reactive oxygen species (ROS) assay kits were purchased from Beyotime Technology (China). Calcein-AM/PI Double Stain Kit Calcein-AM/PI and Viability/Cytotoxicity Assay for Bacteria were provided by US Everbright Inc. (USA). The BCA protein assay kit was purchased from Proteintech Group (China). Anti-IL-6, anti-ly6G and anti-TNF- $\alpha$  antibodies were manufactured by BOSTER Biological Technology (China).

### 2.2. Cells and animals

Members of my research group derived mouse monocyte-macrophage leukaemia cells (RAW264.7 cells) and human umbilical vein endothelial cells (HUVECs) for our study. The cells were cultured in DMEM (high sugar) medium containing 1 % penicillin-streptomycin and 10 % FBS at 37 °C in a 5 % CO<sub>2</sub> humidity incubator. Six-week-old male ICR mice were selected for the study and obtained from the Department of Laboratory Animals, Central South University. All animal experiments were conducted in strict adherence to the Guidelines for the Care and Use of Laboratory Animals and were approved by the Institutional Ethics Committee of Central South University (Ethics Certificate No. CSU-2023-0558).

### 2.3. Bacterial strains

*P. aeruginosa* was collected from inpatients of the Third Xiangya Hospital of Central South University (Changsha, Hunan, China). The bacterial strains were then isolated and stored in bacterial cryopreservative at –80 °C. After recovery, the bacteria were inoculated onto LB agar plates and incubated at 37 °C for 18–24 h. Single colonies were then selected and transferred to LB broth. Samples were incubated overnight at 37 °C with shaking at 200 rpm to facilitate growth to logarithmic phase.

### 2.4. Synthesis of Apt-pM@UCNPmSiO<sub>2</sub>-Cur-CAZ

#### 2.4.1. Detection of macrophage surface receptor expression by flow cytometry

RAW264.7 cells were treated with 0.5  $\mu$ g/mL and 1  $\mu$ g/mL LPS for 12, 24, 36 and 48 h, respectively. The cells were then stained with anti-mouse TLR4 and CD14 antibodies (1:500 dilution in PBS) and incubated for 15–20 min on ice in the dark. After incubation, the cells were washed 2–3 times with PBS and resuspended in PBS. The expression levels of TLR4 and CD14 receptors were analysed by flow cytometry and data analysis was performed using Flow Jo software.

#### 2.4.2. Preparation of Apt-pM

Pre-treated macrophages were collected and placed in ddH<sub>2</sub>O overnight at 4 °C. After being subjected to 8–10 rounds of freeze-thawing, the cells were sonicated on ice (25 min, 42 kHz, 100 W) to fully lyse them. The supernatant was then collected by centrifugation at 1500 rpm for 10 min, and the precipitate was collected by centrifugation at 4 °C and 20,000 g for 30 min, resulting in pM. The F23 aptamer was added to the pM and shaken overnight at room temperature while being protected from light. Centrifugation was then performed to remove any free F23 aptamer. The resulting product was cell membranes with F23 inserted on the surface, known as Apt-pM.

#### 2.4.3. Synthesis of UCNPmSiO<sub>2</sub>-Cur-CAZ

UCNPmSiO<sub>2</sub> was mixed with ceftazidime and curcumin, stirred overnight at room temperature under a magnetic stirrer and protected from light. The resulting precipitate, UCNPmSiO<sub>2</sub>-Cur-CAZ, was collected by centrifugation at 13,000 rpm for 10 min.

#### 2.4.4. Synthesis of Apt-pM@UCNPmSiO<sub>2</sub>-Cur-CAZ

The synthesized Apt-pM was sonicated (5 min, 42 kHz, 100 W) with an equal volume of UCNPmSiO<sub>2</sub>-Cur-CAZ. The excess Apt-pM was removed by centrifuging at 2500 rpm for 10 min. The Apt-pM@UCNPmSiO<sub>2</sub>-Cur-CAZ nanocomplexes were then formed and stored at 4 °C for backup.

#### 2.4.5. Characterization

The size and morphology of UCNPmSiO<sub>2</sub>, pM and pM@UCNPmSiO<sub>2</sub> were observed by the transmission electron microscopy (TEM) with a Tecnai G2 Spirit TEM (FEI). Elemental mapping analyses were performed using a FEI Talos F200x with an integrated Super-X EDS system (FEI, USA). The pM membrane proteins were identified by SDS-PAGE. Zetasizer Nano ZS (Malvern Nano Series, Malvern, UK) was used to determine the dynamic light scattering (DLS) and zeta potential of UCNPmSiO<sub>2</sub>, pM, and pM@UCNPmSiO<sub>2</sub>. The successful synthesis of Apt-pM@UCNPmSiO<sub>2</sub>-Cur-CAZ was verified by UV-Vis spectrometry (ScanDrop, Analytik Jena, Germany).

#### 2.4.6. In vitro antimicrobial assay

Five treatment groups (UCNPmSiO<sub>2</sub>, Cur, CAZ, UCNPmSiO<sub>2</sub>-Cur-CAZ, Apt-pM@UCNPmSiO<sub>2</sub>-Cur-CAZ) were administered at a uniform concentration of 20 µg/mL.

#### 2.4.7. Disk diffusion method

From overnight shaking culture to logarithmic growth phase, the bacterial suspension was adjusted to 0.5 MCF using MH medium and evenly spread onto MH agar plates. The Paper was placed on the surface of the plate and treated with different drugs. The incubation was carried out at 37 °C with 5 % CO<sub>2</sub> for 16–18 h, and the size of the inhibition circle was observed.

#### 2.4.8. Reactive oxygen species (ROS) assay

Bacteria were treated with the corresponding materials for 10 h. After treatment, a final concentration of 10 µmol/L DCFH-DA was added and incubated for 20 min at 37 °C, protected from light. The amount of ROS production was assessed by detecting fluorescence signals using a fluorescence zymograph and flow cytometer at 488 nm (excitation wavelength) and 525 nm (emission wavelength).

#### 2.4.9. Confocal laser scanning microscope (CLSM) assay of LIVE/DEAD bacteria

The bacteria were incubated until late logarithmic growth and then treated with appropriate drugs for 24 h. The bacterial precipitate was obtained by centrifugation at 5000g for 15 min. Next, 10 µL of a bacterial LIVE/DEAD detection kit consisting of NucGreen and EthD-III was added to 1 mL of bacterial suspension. The staining process was carried out for 15 min at room temperature in a dark environment.

Subsequently, fluorescence images were captured using CLSM (Zeiss LSM 800, Germany).

#### 2.4.10. Scanning electron microscope (SEM) observation of *P. aeruginosa*

After 24 h of incubation with different drugs, the bacteria were centrifuged at 10,000 rpm for 3 min. The precipitates were then washed 3–5 times with sterile PBS solution and fixed with 2.5 % glutaraldehyde and 0.1 mol/L cocoate buffer (pH = 7.4) at 4 °C overnight. After another 10 min of incubation with 0.2 mol/L cocoate buffer (pH = 7.4), they were washed 2–3 times with PBS solution. Dehydration was carried out using four ethanol gradients (30 %, 50 %, 70 %, and 90 %) for 10 min each. The samples were then dehydrated twice using anhydrous ethanol for 10 min each. After air-drying for 24 h, a 7 nm thick layer of gold-palladium was coated on the samples, and the bacterial morphology was observed using SEM (HITACHI Regulus 8100).

#### 2.4.11. Bacterial biofilm detection

**2.4.11.1. CLSM assay.** A bacterial suspension of 2 mL was added to a laser confocal petri dish and incubated at 37 °C for 36–48 h. Once the biofilm was formed, the corresponding drug was added and treated for 24 h. Subsequently, a bacterial LIVE/DEAD staining kit was added and incubated for 15 min at room temperature, protected from light. Finally, 3D pictures were taken with CLSM.

**2.4.11.2. Crystalline violet staining.** In a 96-well plate, 100 µL of bacterial suspension was added, followed by 100 µL of the corresponding treatment drug, and incubated at 37 °C for 24 h. The plate was washed 3 times with PBS, and 100 µL of methanol was fixed for 15 min, then the excess methanol was aspirated. After drying, 200 µL of 1 % crystal violet solution was added and incubated at room temperature for 15 min, then the excess crystal violet dye was aspirated and washed 3 times with PBS. Next, 200 µL of 95 % ethanol was added to dissolve the crystal violet. The solution was then incubated for 20 min at room temperature, and the absorbance value was measured at 570 nm using a Multifunctional Enzyme Labelling Instrument (PerkinElmer EnSpire, USA).

**2.4.11.3. Targeting validation.** After an overnight incubation of *P. aeruginosa*, the bacteria were co-incubated with NucGreen green fluorescent dye for 20 min. They were then centrifuged at 10,000 rpm for 3 min and resuspended in sterile PBS. The cy5-labelled UCNPmSiO<sub>2</sub>-Cur-CAZ, pM@UCNPmSiO<sub>2</sub>-Cur-CAZ and Apt-pM@UCNPmSiO<sub>2</sub>-Cur-CAZ were mixed with the bacteria for 3 h. Finally, the images were collected by CLSM.

**2.4.11.4. Biocompatibility of Apt-pM@UCNPmSiO<sub>2</sub>-Cur-CAZ in vitro.** Five treatment groups (UCNPmSiO<sub>2</sub>, Cur, CAZ, UCNPmSiO<sub>2</sub>-Cur-CAZ, Apt-pM@UCNPmSiO<sub>2</sub>-Cur-CAZ) were administered at a uniform concentration of 20 µg/mL.

**2.4.11.5. Hemocompatibility.** Different concentrations (2, 4, 8, 16, 32, 64 and 128 µg/mL) of UCNPmSiO<sub>2</sub> and pM@UCNPmSiO<sub>2</sub> were incubated with 5 % erythrocyte suspension for 2 h at 37 °C. After centrifugation at 3500 rpm for 5 min, haemolysis was observed and recorded. The supernatant was collected and the rate of haemolysis was calculated by measuring the absorbance at 545 nm using a Multifunctional Enzyme Labelling Instrument. Positive and negative controls were ddH<sub>2</sub>O and PBS, respectively. The haemolysis rate can be calculated using the following formula: (absorbance value of the experimental group - absorbance value of the negative control)/(absorbance value of the positive control - absorbance value of the negative control) × 100 %.

**2.4.11.6. Cytotoxicity assay.** After inoculating 100 µL of cell suspension per well in a 96-well plate for 24 h, 10 µL of UCNPmSiO<sub>2</sub> and pM@UCNPmSiO<sub>2</sub> at different concentrations (2, 4, 8, 16, 32, 64 and

128 µg/mL) were added to the wells for 24 h. Following this, 10 µL of CCK-8 was added to each well and the plate was incubated for 3 h. Finally, the absorbance of the wells at 450 nm was measured. Cell survival = (absorbance of experimental wells - absorbance of blank wells)/(absorbance of control wells - absorbance of blank wells) × 100 %.

**2.4.11.7. Detection of apoptosis.** After 24 h of treatment with the corresponding materials, the cells were collected and resuspended in 1 × Binding Buffer. The Annexin V-FITC/PI Apoptosis Detection Kit was added, and the cells were incubated at room temperature, protected from light, for 20 min. The apoptosis rate of HUVECs was immediately detected by flow cytometry.

**2.4.11.8. ROS detection.** After incubating each treatment group with HEUVCs for 24 h, cell precipitates were collected and suspended in the fluorescent probe DCFH-DA (diluted 1:1000 with serum-free medium) and incubated in a cell culture incubator at 37 °C for 20 min. The cells were washed 3 times with serum-free cell culture medium, and ROS produced by the cells were detected by flow cytometry.

**2.4.11.9. LIVE/DEAD cell staining.** HEUVCs were inoculated in 6-well plates with the corresponding treatment groups and incubated at 37 °C and 5 % CO<sub>2</sub> for 24 h. After washing the cells 2–3 times with PBS, Calcein-AM/PI staining working solution was added and the cells were incubated at room temperature and protected from light for 15 min. Finally, the cells were observed using a fluorescence microscope (Carl Zeiss, Germany).

**2.4.11.10. Mice model of *P. aeruginosa* skin wound infection.** Twenty-eight 6-week-old male ICR mice were randomly divided into 7 groups: the PBS group, the UCNPmSiO<sub>2</sub> group, the curcumin group, the ceftazidime group, the UCNPmSiO<sub>2</sub>-Cur-CAZ group, the Apt-pM@UCNPmSiO<sub>2</sub>-Cur-CAZ group, and the NIR irradiated Apt-pM@UCNPmSiO<sub>2</sub>-Cur-CAZ group. Modelling was started after one week of acclimatization feeding. The mice were positioned prone and their back hair was shaved. The surgical site was disinfected before creating a circular full skin defect wound with a diameter of 10 mm on the dorsal surface using a circular skin punch. Following this, 50 µL of *P. aeruginosa* bacterial suspension (1 × 10<sup>6</sup> CFU/mL) was added to the wound surface. The corresponding treatment group's solution was injected onto the wound surface one day later. The Apt-pM@UCNPmSiO<sub>2</sub>-Cur-CAZ group was irradiated with NIR light at the wound site for 10 min with a power of 1 W/cm<sup>2</sup>. Wound healing progress was recorded, and the wound diameter was measured on days 0, 2, 5, 9, and 12.

On the twelfth day, tissue fluid was collected from the wound using a sterile specimen. The fluid was then added to LB medium and incubated at 37 °C for 24 h. After incubation, the culture fluid was evenly spread on NA plates and the colonies were counted after 18–24 h. The mice were euthanised, and the wound site and surrounding healthy skin tissues were taken and spread flat. They were then placed in 4 % paraformaldehyde tissue fixative for fixation and preservation. HE staining and Masson staining were conducted on the tissues at the wound site. Simultaneously, immunohistochemical staining was performed to detect the expression of TNF-α, IL-6, and Ly6G.

Six treatment groups (UCNPmSiO<sub>2</sub>, Cur, CAZ, UCNPmSiO<sub>2</sub>-Cur-CAZ, Apt-pM@UCNPmSiO<sub>2</sub>-Cur-CAZ, Apt-pM@UCNPmSiO<sub>2</sub>-Cur-CAZ + NIR) were administered at a uniform concentration of 20 µg/mL.

**2.4.11.11. In vivo toxicity assessment.** Twenty-four male ICR mice were divided into six groups of four mice each. Each group was injected with 100 µL of a different substance through the tail vein: PBS, UCNPmSiO<sub>2</sub>, curcumin, ceftazidime, UCNPmSiO<sub>2</sub>-Cur-CAZ, and Apt-pM@UCNPmSiO<sub>2</sub>-Cur-CAZ. The body weights of the mice were then monitored and recorded every two days. Haematological and biochemical indicators were detected using whole blood and serum collected after 12 days. The

indices included red blood count (RBC), white blood count (WBC), haemoglobin (Hb), platelet count (PLT), alanine aminotransferase (ALT), aspartate aminotransferase (AST), blood urea nitrogen (BUN), and creatinine (CREA). Following blood collection, each ICR mouse was euthanised by cervical dislocation. The major internal organs, including the heart, liver, spleen, lungs, and kidneys, were collected and analysed for pathological structures using HE staining. The structures were then photographed under microscopic observation.

Six treatment groups (UCNPmSiO<sub>2</sub>, Cur, CAZ, UCNPmSiO<sub>2</sub>-Cur-CAZ, Apt-pM@UCNPmSiO<sub>2</sub>-Cur-CAZ, Apt-pM@UCNPmSiO<sub>2</sub>-Cur-CAZ + NIR) were administered at a uniform concentration of 20 µg/mL.

**2.4.11.12. Statistical analysis.** The data were analysed using GraphPad Prism. The measurements were expressed as mean ± standard deviation (mean ± SD). Comparisons between groups were assessed using one-way ANOVA, Tukey's post-test, and differences were considered statistically significant at *p* < 0.05.

### 3. Results and discussion

#### 3.1. Macrophage surface receptor expression

To determine the optimal concentration and duration of LPS stimulation for high expression of macrophage surface receptors, macrophages were stimulated with varying concentrations of *P. aeruginosa*-derived LPS for different durations. The surface expression of TLR4 and CD14 on macrophages was then detected using flow cytometry. TLR4 expression increased gradually with prolonged LPS stimulation, while CD14 expression was highest after 24 h of stimulation (Fig. 1A and B). Stimulation of macrophages with different concentrations (0.5 and 1 µg/mL) of LPS for the same duration did not result in significant differences in receptor expression. After 24 h of stimulation, cell survival was higher than 70 % with both 0.5 and 1 µg/mL LPS (Fig. S1). However, after 48 h of stimulation, only 10.3 % and 1.5 % of the cells survived with 0.5 and 1 µg/mL LPS, respectively (Fig. S1). To achieve high expression of surface receptors while minimizing toxicity to macrophages, we extracted cell membranes from macrophages stimulated with 0.5 µg/mL LPS for 24 h.

#### 3.2. Characterization of Apt-pM@UCNPmSiO<sub>2</sub>-Cur-CAZ nanosystems

Fig. 2A showed that the particle size of the synthesized UCNPmSiO<sub>2</sub> is approximately 50 ± 5 nm with a uniform distribution. Each nanoparticle has a distinct core-shell structure with a visible silica shell layer and is uniformly circular. Compared with the that of pM@UCNPmSiO<sub>2</sub>, the morphological features of Apt-pM@UCNPmSiO<sub>2</sub>-Cur-CAZ did not significantly change (Fig. S2A). The successful synthesis of lanthanide doped upconverted nanomaterials with successful encapsulation of pM is indicated by the co-localisation of phosphorus (P), silicon (Si), yttrium (Y), ytterbium (Yb) and thulium (Tm) elements, as shown in Fig. 2B EDS elemental mapping analysis. Fig. 2C showed the protein composition of pM and pM@UCNPmSiO<sub>2</sub> by SDS-PAGE. The results indicated that pM@UCNPmSiO<sub>2</sub> and pM cell membranes had similar protein profiles, confirming the successful encapsulation of pM. Fig. 2D and E showed that the particle size of UCNPmSiO<sub>2</sub> was detected by DLS to be about 155 nm, and the particle size of pM@UCNPmSiO<sub>2</sub> was about 285 nm after pM encapsulation. In addition, it was obviously that the mean particle diameter of Apt-pM@UCNPmSiO<sub>2</sub>-Cur-CAZ was approximately nm 281.21 ± 3.31 nm (Fig. S2B). The increase in the DLS results compared to those of TEM may be due to the fact that the samples contained a small number of large particles or the occurrence of agglomeration of the nanoparticles, which led to the high detection results of the DLS particle size. The Zeta potentials of UCNPmSiO<sub>2</sub>, pM, pM@UCNPmSiO<sub>2</sub>, and Apt-pM@UCNPmSiO<sub>2</sub>-Cur-CAZ were -15.7 mV, 6.5 mV, -0.8 mV, and -25.75 mV, respectively (Fig. 2F and Fig. S2C). It

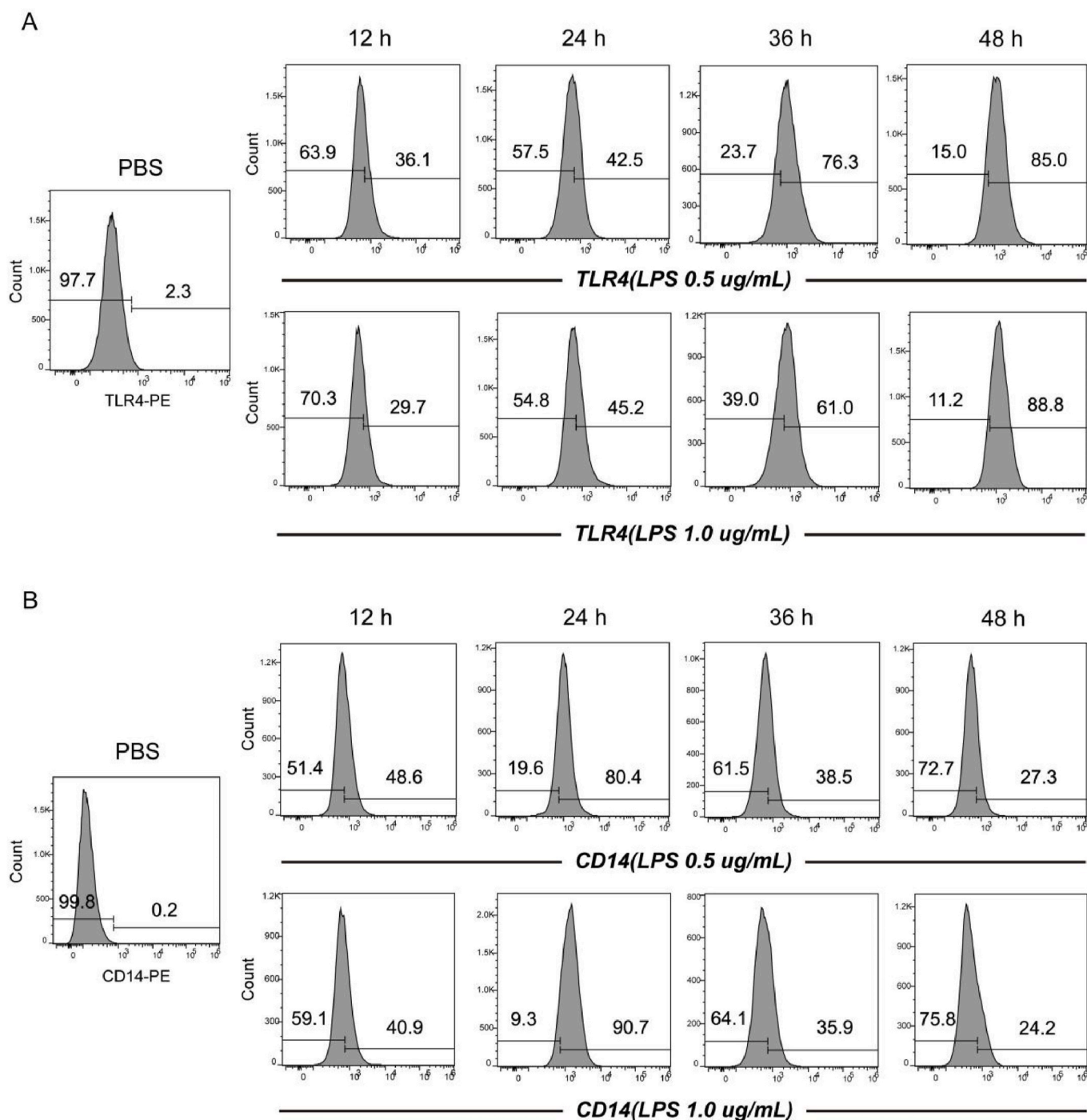


Fig. 1. Flow cytometric detection of macrophage surface receptor expression. (A) Expression of TLR4. (B) Expression of CD14.

could be observed that the potential of pM@UCNPmSiO<sub>2</sub> increased compared to UCNpMsiO<sub>2</sub> when pM was encapsulated. This was due to the positively charged cell membrane neutralising the negative charge on the surface of UCNpMsiO<sub>2</sub>. The UV–Vis analysis in Fig. 2G indicated that Apt-pM@UCNPmSiO<sub>2</sub>-Cur-CAZ exhibited absorption peaks at 217 nm, 238 nm, 435 nm, and 256 nm. These peaks corresponded to the characteristic absorption peaks of pM, UCNpMsiO<sub>2</sub>, curcumin, and ceftazidime, respectively, confirming the successful synthesis of Apt-pM@UCNPmSiO<sub>2</sub>-Cur-CAZ. The encapsulation efficiency of curcumin in UCNpMsiO<sub>2</sub>-Cur-CAZ was about 75.5 % and the loading rate was about 28.0 %; the encapsulation efficiency of ceftazidime was about 46.6 % with a loading rate of about 16.0 % (Fig. S3A). At pH = 6.5, the 48h

release rate of curcumin was 74.7 %, while at pH = 7.4 the release rate was only 32.3 % (Fig. S3B). Ceftazidime had a release rate of 53.4 % after 48 h at pH 6.5, while at pH 7.4, the release rate was only 13.7 % (Fig. S3C). Therefore, this study demonstrates that Apt-pM@UCNPmSiO<sub>2</sub>-Cur-CAZ nanosystems are pH-sensitive nanocomposites that improve the release of loaded drugs.

### 3.3. *In vitro* antibacterial effect of Apt-pM@UCNPmSiO<sub>2</sub>-Cur-CAZ

The results of the paper diffusion method showed that both UCNpMsiO<sub>2</sub>-Cur-CAZ and Apt-pM@UCNPmSiO<sub>2</sub>-Cur-CAZ exhibited significant inhibition with an increased inhibition circle diameter of

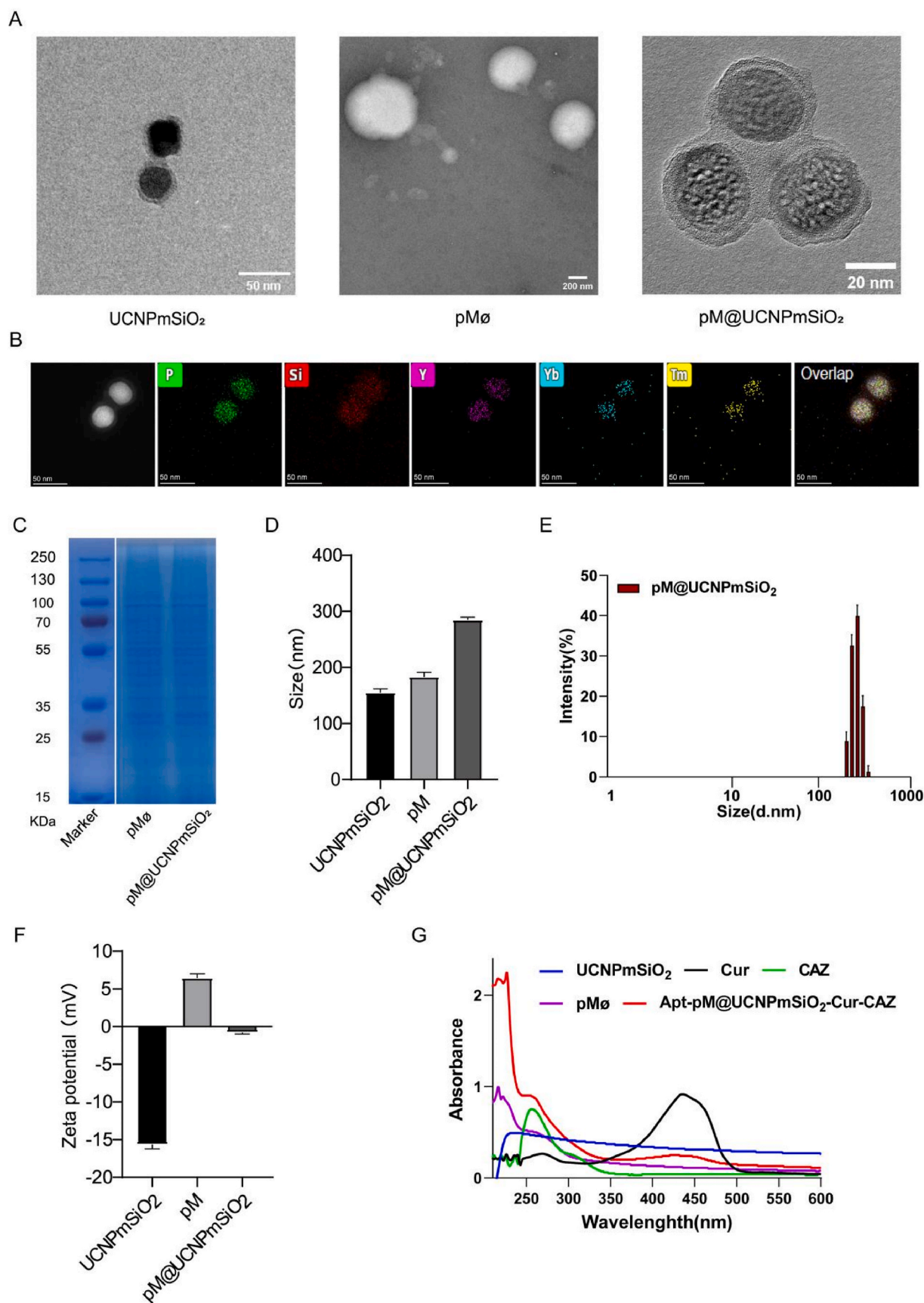


**Fig. 2.** Characterization of Apt-pM@UCNPs@SiO<sub>2</sub>-Cur-CAZ. (A) TEM images of UCNPs@SiO<sub>2</sub>, pM and pM@UCNPs@SiO<sub>2</sub>. (B) Element mapping of pM@UCNPs@SiO<sub>2</sub> using TEM. (C) SDS-PAGE protein assessment. (D) and (E) DLS analysis of UCNPs@SiO<sub>2</sub>, pM and pM@UCNPs@SiO<sub>2</sub>. (F) Zeta potential values of UCNPs@SiO<sub>2</sub>, pM and pM@UCNPs@SiO<sub>2</sub>. (G) UV-Vis spectra of UCNPs@SiO<sub>2</sub>, Cur, CAZ, pMø and Apt-pM@UCNPs@SiO<sub>2</sub>-Cur-CAZ.

approximately 24 mm compared to the PBS group (Fig. 3A and B). As showed in Fig. S4, the diameter of the inhibition zone was  $22.1 \pm 0.3$  mm in Cur-CAZ group. The inhibition zones of curcumin and ceftazidime were respectively less than that of Cur-CAZ, which proved the synergistic antibacterial effect between curcumin and ceftazidime. Thus, the inhibition zones of pM@UCNPmSiO<sub>2</sub>-Cur-CAZ and Apt-pM@UCNPmSiO<sub>2</sub>-Cur-CAZ were larger than that of ceftazidime. The level of ROS expression was measured using the DCFH-DA fluorescent probe following treatment of *P. aeruginosa* with the respective materials. The results indicated a significant increase in ROS levels after treatment with UCNpMsiO<sub>2</sub>-Cur-CAZ and Apt-pM@UCNPmSiO<sub>2</sub>-Cur-CAZ (Fig. 3C and D). To further detect the elevation of ROS in Apt-pM@UCNPmSiO<sub>2</sub>-Cur-CAZ + NIR group by fluorescence intensity (Fig. S5C) and flow cytometry (Fig. S5D), it was obviously that the increase amounts of ROS in it were the most in all seven groups (PBS, UCNpMsiO<sub>2</sub>, curcumin, ceftazidime, UCNpMsiO<sub>2</sub>-Cur-CAZ, Apt-pM@UCNPmSiO<sub>2</sub>-Cur-CAZ, and Apt-pM@UCNPmSiO<sub>2</sub>-Cur-CAZ + NIR). To research the antibacterial activity against *P. aeruginosa*, the treated *P. aeruginosa* samples were stained with NueGreen and EthD-III fluorochromes, and then captured by CLSM to form images. Regarding the LIVE/DEAD backlight bacterial viability kit, the NueGreen fluorochrome would only stain the live bacteria to show green fluorescence. The dead bacteria could be stained with NueGreen and EthD-III fluorochromes simultaneously to exhibit green and red fluorescence at different excitation wavelengths. The fluorescence images (Fig. 3E) showed that the UCNpMsiO<sub>2</sub>-Cur-CAZ and Apt-pM@UCNPmSiO<sub>2</sub>-Cur-CAZ groups had the highest number of dead bacteria and the most significant bacterial inhibition effect. However, with the use of NIR light, the number of dead bacteria further increased in Apt-pM@UCNPmSiO<sub>2</sub>-Cur-CAZ + NIR group (Fig. S5A). SEM was used to observe the morphology and damage of *P. aeruginosa* following treatment with various groups. The bacteria in the PBS group were observed to be bluntly rounded at both ends and had a regular structure (Fig. 3F). However, after treated with UCNpMsiO<sub>2</sub>-Cur-CAZ and Apt-pM@UCNPmSiO<sub>2</sub>-Cur-CAZ, the bacteria appeared to have different degrees of concavity and wrinkles, and the morphology was disorganised, indicating that the bacteria had undergone serious damage (Fig. 3F). As the image of SEM distinctly displayed, all bacteria began to break into pieces with the use of NIR light for Apt-pM@UCNPmSiO<sub>2</sub>-Cur-CAZ (Fig. S5B). It was obviously that the antibacterial effect was strongest in Apt-pM@UCNPmSiO<sub>2</sub>-Cur-CAZ + NIR group, due to the photodynamic characteristic of Apt-pM@UCNPmSiO<sub>2</sub>-Cur-CAZ nanocomposite.

The study evaluated the damage to biofilm caused by different materials using LIVE/DEAD bacterial viability staining. The 3D images obtained by CLSM (Fig. 4A and Figure S5H) showed that the Apt-pM@UCNPmSiO<sub>2</sub>-Cur-CAZ + NIR group had the strongest red fluorescence among the seven groups (PBS, UCNpMsiO<sub>2</sub>, curcumin, ceftazidime, UCNpMsiO<sub>2</sub>-Cur-CAZ, Apt-pM@UCNPmSiO<sub>2</sub>-Cur-CAZ, and Apt-pM@UCNPmSiO<sub>2</sub>-Cur-CAZ + NIR), reflecting the highest number of dead biofilms. This suggested that the synthesized nanosystems could damage the biofilm of *P. aeruginosa* with photodynamic therapy. The inhibition efficiency of various treatment groups against *P. aeruginosa* biofilm was assessed using crystal violet staining. Compared with the Apt-pM@UCNPmSiO<sub>2</sub>-Cur-CAZ alone (Fig. 5B), the effect of biofilm inhibition was much well in Apt-pM@UCNPmSiO<sub>2</sub>-Cur-CAZ + NIR group (Figure S5E and Figure S5F). The biofilm inhibition percentage of Apt-pM@UCNPmSiO<sub>2</sub>-Cur-CAZ + NIR was as high as 94 % or more (Fig. S5G), and that was most in seven treatments. The relative percentage of bacterial biofilm inhibition was calculated based on the absorbance values, and both the UCNpMsiO<sub>2</sub>-Cur-CAZ and Apt-pM@UCNPmSiO<sub>2</sub>-Cur-CAZ groups exhibited 88.9 % and 89.3 % inhibition of bacterial biofilm, respectively (Fig. 5B). In conclusion, the nanosystem was shown to effectively inhibit the formation of bacterial biofilm and the effect was much stronger with the use of NIR light.

To verify the effectiveness of pre-treated macrophage membranes with aptamer sequences encapsulated with nanoparticles, we co-

cultivated a certain concentration of cy5-labelled UCNpMsiO<sub>2</sub>-Cur-CAZ, pM@UCNPmSiO<sub>2</sub>-Cur-CAZ and Apt-pM@UCNPmSiO<sub>2</sub>-Cur-CAZ with NueGreen-stained *P. aeruginosa* for 3 h. CLSM images were then obtained. As shown in Fig. 4C, encapsulating the pre-treated macrophage membrane provided a targeting effect to the nanosystem. After insertion of the aptamer sequence, more bacteria bound to the surface of the nanoparticles, indicating that the nanosystem had a good ability to target the bacteria and could better inhibit bacterial growth.

#### 3.4. In vitro biocompatibility of Apt-pM@UCNPmSiO<sub>2</sub>-Cur-CAZ

To evaluate the haemocompatibility of the novel nanosystems constructed, a haemolysis test was performed in this study. Erythrocytes (5 %) were incubated with varying concentrations of UCNpMsiO<sub>2</sub> and pM@UCNPmSiO<sub>2</sub> (2, 4, 8, 16, 32, 64 and 128 µg/mL) for 2 h. As depicted in Fig. 5A and B, the haemolysis rate of mice remained low (less than 2 % for both) even as the concentration of UCNpMsiO<sub>2</sub> and pM@UCNPmSiO<sub>2</sub> increased. The study found that UCNpMsiO<sub>2</sub> had good haemocompatibility itself, and the haemolysis rate of pM@UCNPmSiO<sub>2</sub> was lower than that of UCNpMsiO<sub>2</sub> after encapsulation of macrophage membranes, suggesting that encapsulation of natural biofilm would improve the biocompatibility of UCNpMsiO<sub>2</sub>.

To evaluate the in vitro biocompatibility of the nanomaterials, we selected HUVECs. The cells were treated with varying concentrations (2, 4, 8, 16, 32, 64, and 128 µg/mL) of UCNpMsiO<sub>2</sub> and pM@UCNPmSiO<sub>2</sub> for 24 h. The number of viable cells was then determined using a CCK-8 kit. Fig. 5C showed that the cell viability of both groups was still higher than 80 % when the nanomaterial concentration was 128 µg/mL, indicating that the UCNpMsiO<sub>2</sub> and pM@UCNPmSiO<sub>2</sub> nanocomposites were not significantly cytotoxic.

The impact of the materials on apoptosis was analysed using flow cytometry. It was noteworthy that the apoptosis rate of all six treatment groups was less than 5 %, indicating that the effect of Apt-pM@UCNPmSiO<sub>2</sub>-Cur-CAZ nanocomposites and some of the free drugs on normal cells was negligible (Fig. 5D). The ROS content was evaluated using DCFH-DA. The flow cytometry detection images indicated that the ROS content remained low in all treatment groups after treating HUVECs. This suggested that the Apt-pM@UCNPmSiO<sub>2</sub>-Cur-CAZ nanosystems did not cause any significant alterations to the normal state of the cells (Fig. 5E).

Cell survival was assessed using the LIVE/DEAD Staining Kit. Live cells were stained with calcein, producing green fluorescence, while dead cells were stained with the PI fluorescent probe, producing red fluorescence. The intensity of red fluorescence was weaker in the 6 treatment groups, indicating that the HUVECs were in good condition (Fig. 5F). In conclusion, the Apt-pM@UCNPmSiO<sub>2</sub>-Cur-CAZ nanosystem constructed were found to be highly biocompatible, with no significant cytotoxicity observed.

#### 3.5. Apt-pM@UCNPmSiO<sub>2</sub>-Cur-CAZ promotes skin wound healing effect

To assess the therapeutic efficacy of Apt-pM@UCNPmSiO<sub>2</sub>-Cur-CAZ in vivo, a skin wound model of *Pseudomonas aeruginosa*-infected mice was established, as shown in Fig. 6A. The corresponding treatment groups were topically administered on the wound surface. The entire treatment period was completed in 12 days. Fig. 6B and C demonstrated that the control wounds remained pus-filled, red, and swollen on day 8, with 60.7 % of the wounds still unhealed on day 12. In contrast, the wounds treated with Apt-pM@UCNPmSiO<sub>2</sub>-Cur-CAZ showed no signs of inflammation, formed scabs after 9 days of treatment, and had an 85.3 % healing rate on day 12. In the group treated with Apt-pM@UCNPmSiO<sub>2</sub>-Cur-CAZ and irradiated with NIR, the wound size was significantly reduced by the 5th day, with no signs of pus or inflammation. Scabs had formed by the 9th day, resulting in the smallest defect, and the wound was almost completely healed by the 12th day, with a healing rate of 94.9 %. This treatment resulted in the fastest and most effective healing.

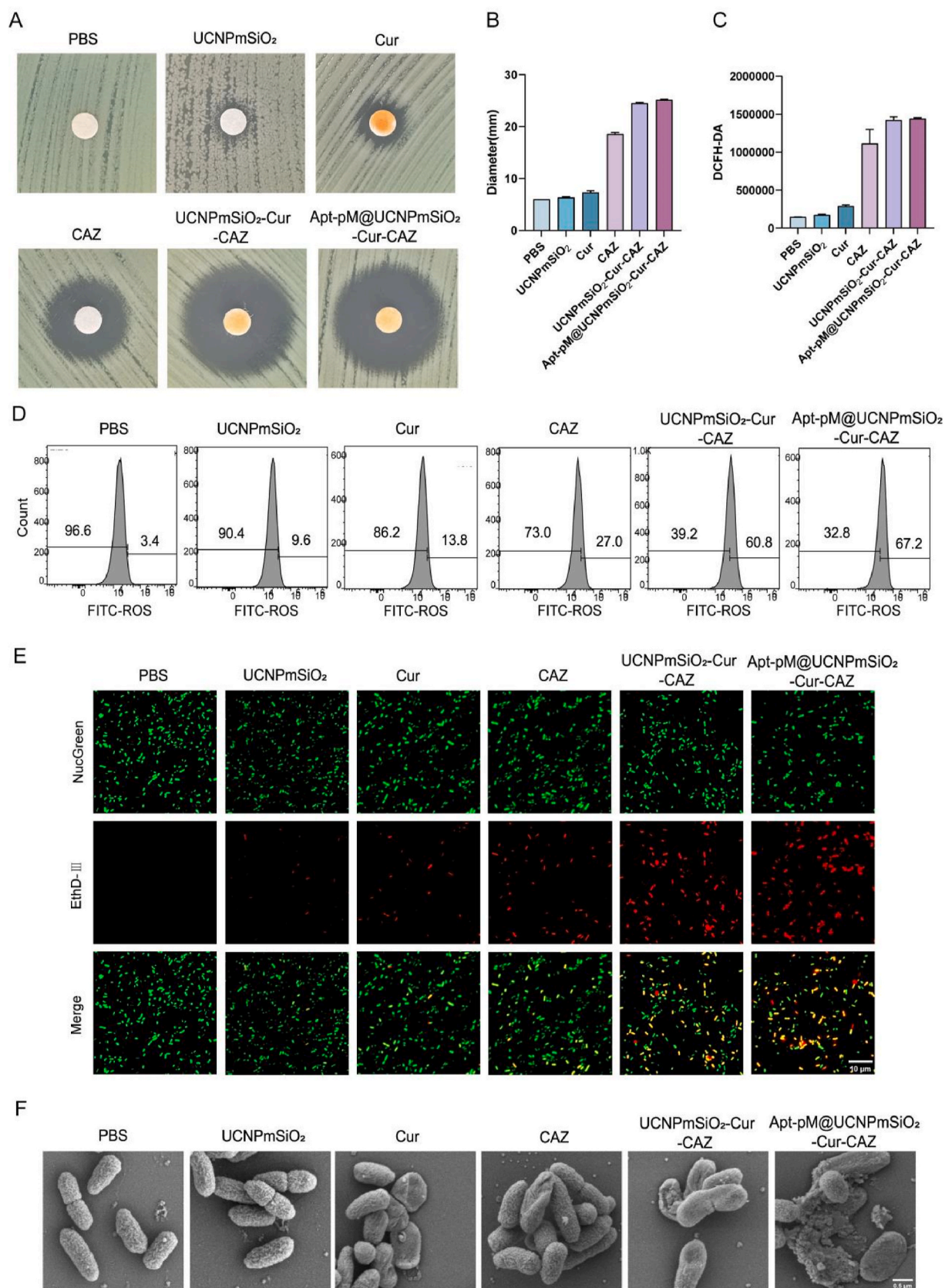


**Fig. 3.** In vitro antibacterial effect of Apt-pM@UCNPmsio<sub>2</sub>-Cur-CAZ. (A) Inhibition zones and (B) corresponding inhibition zone diameters of different treatment groups against *P. aeruginosa*. (C) Fluorescence zymography and (D) Flow cytometry were used to detect the level of ROS following treatment of *P. aeruginosa* with various treatment groups. (E) CLSM images of *P. aeruginosa* upon six various treatments for 24 h. Scale bar: 10  $\mu$ m. (F) Morphologic observations of *P. aeruginosa* exposed to the respective treatments for 24 h by SEM. Scale bar: 0.5  $\mu$ m.



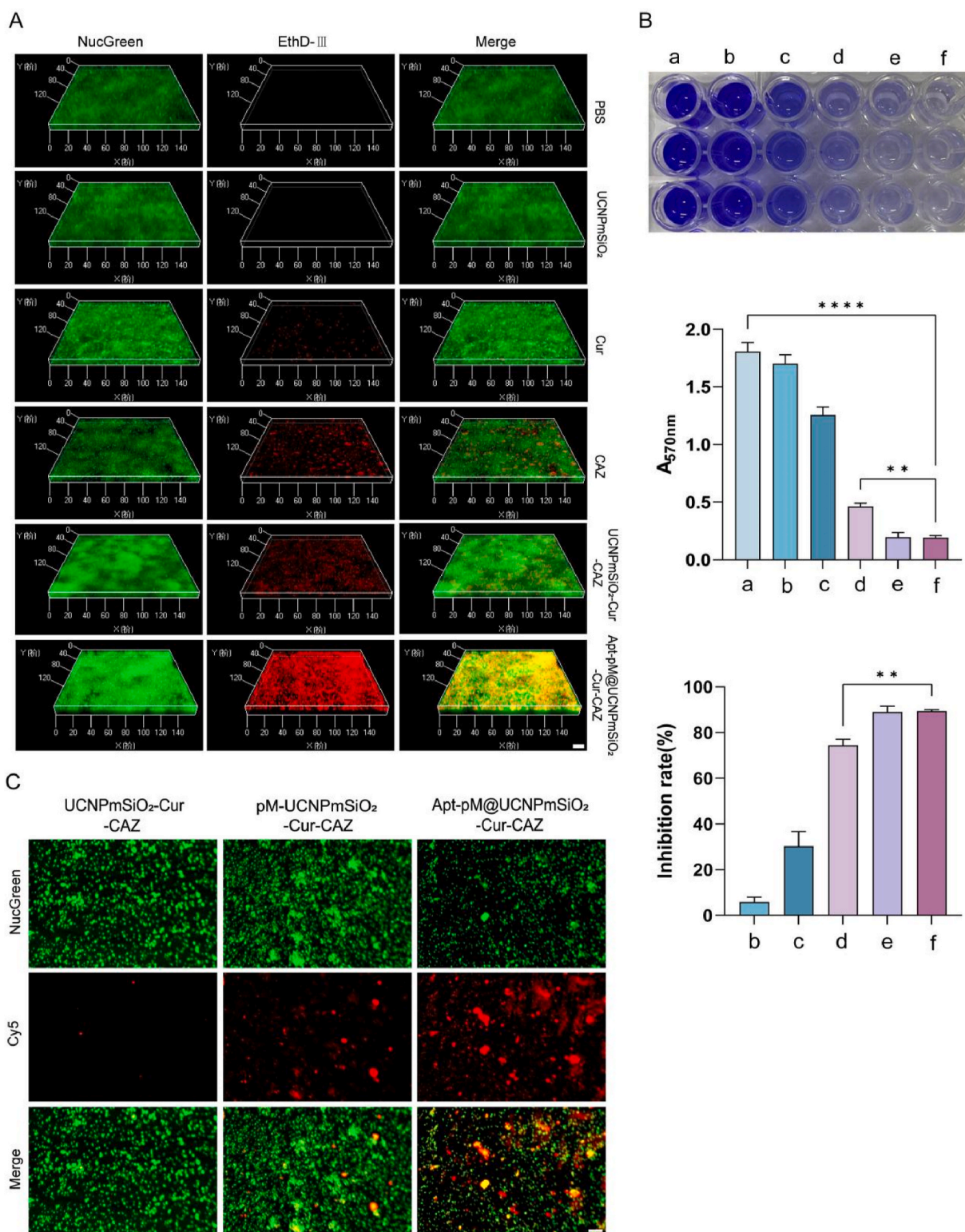
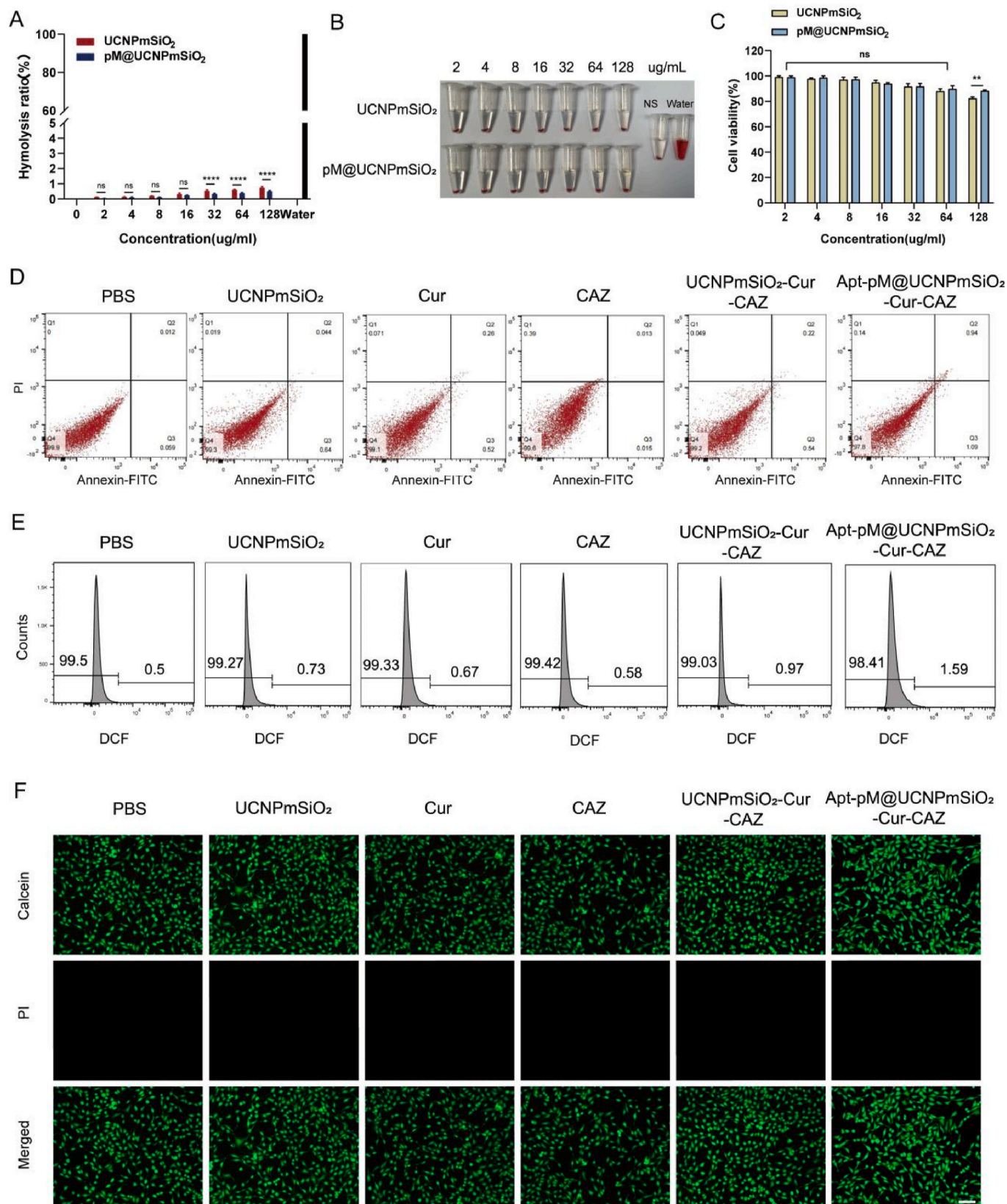


**Fig. 4.** Anti-biofilm activity and targetability of Apt-pM@UCNPmSiO<sub>2</sub>-Cur-CAZ. (A) CLSM images of *P. aeruginosa* biofilm. Scale bar: 20 μm. (B) Crystal violet staining assay images of *P. aeruginosa* biofilms, along with corresponding absorbance values at 570 nm and average inhibition percentage of biofilm treated with different treatments. (C) CLSM images of *P. aeruginosa* incubated with UCNPmSiO<sub>2</sub>-Cur-CAZ, pM@UCNPmSiO<sub>2</sub>-Cur-CAZ and Apt-pM@UCNPmSiO<sub>2</sub>-Cur-CAZ. Scale bar: 50 μm \*\**p* < 0.01, \*\*\*\**p* < 0.0001. (For interpretation of the references to colour in this figure legend, the reader is referred to the Web version of this article.)

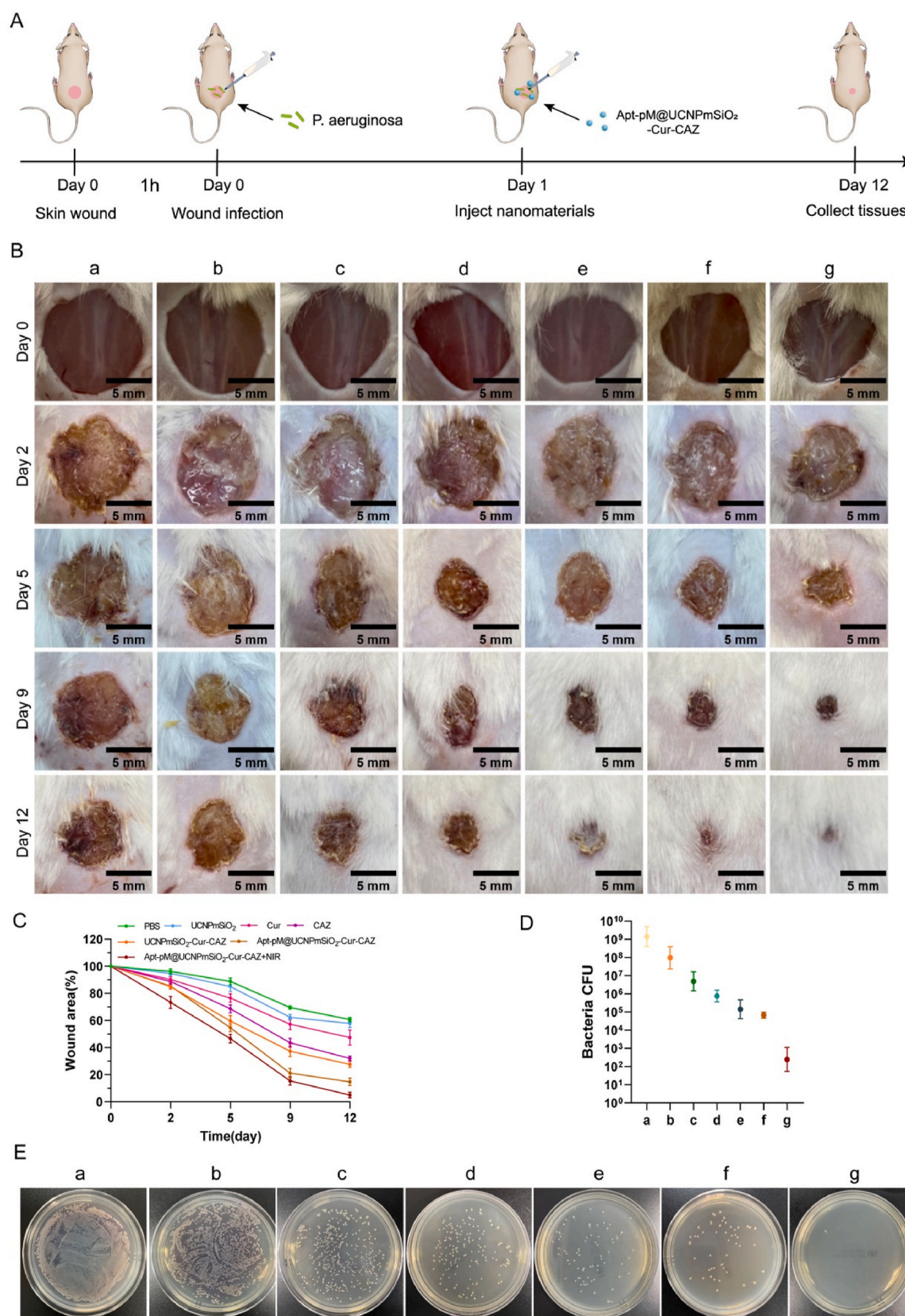
Fig. 6D and E showed that the number of bacteria in the NIR-irradiated Apt-pM@UCNPmSiO<sub>2</sub>-Cur-CAZ group was significantly lower than that in the PBS group, indicating a strong bacterial inhibition effect.

Fig. 7A showed Masson staining of skin wound tissue to observe collagen deposition. Collagen fibres were stained in blue and it can be

seen that the NIR-irradiated Apt-pM@UCNPmSiO<sub>2</sub>-Cur-CAZ group had significantly more collagen fibres, which were arranged in a regular and orderly manner, with better wound repair. The PBS group had only a small number of collagen fibres, which were sparse and disordered. The study observed pathological changes in the wound tissue of mice



**Fig. 5.** In vitro biocompatibility of Apt-pM@UCNPmSiO<sub>2</sub>-Cur-CAZ. (A) Hemolysis ratios of RBC suspensions after treatment with UCNPmSiO<sub>2</sub> and pM@UCNPmSiO<sub>2</sub> at the different concentrations for 3 h and (B) Images. (C) Viability of HUVECs treated with UCNPmSiO<sub>2</sub> and pM@UCNPmSiO<sub>2</sub> at the different concentrations. (D) The apoptosis rates of HUVECs were measured after 24 h of different treatment by flow cytometry. (E) Flow cytometry was used to determine ROS levels in HUVECs after 24 h with different treatments. (F) Live/dead situation of HUVECs with the different treatments for 24 h using calcein and PI fluorescence dye. Scale bar: 50 μm \*\**p* < 0.01, \*\*\*\**p* < 0.0001, ns = no significance.



**Fig. 6.** Apt-pM@UCNPmSiO<sub>2</sub>-Cur-CAZ promotes skin wound healing in vivo. (A) Pattern diagram of the model of skin wounds infected with *P. aeruginosa*. (B) Images of skin wounds on days 0, 2, 5, 9 and 12. Scale bar: 5 mm. (C) Ratio of infected wounds area. Measurement expresses wound area as a percentage of initial wound area. (D) and (E) Skin wound bacterial colony counts after various treatments.

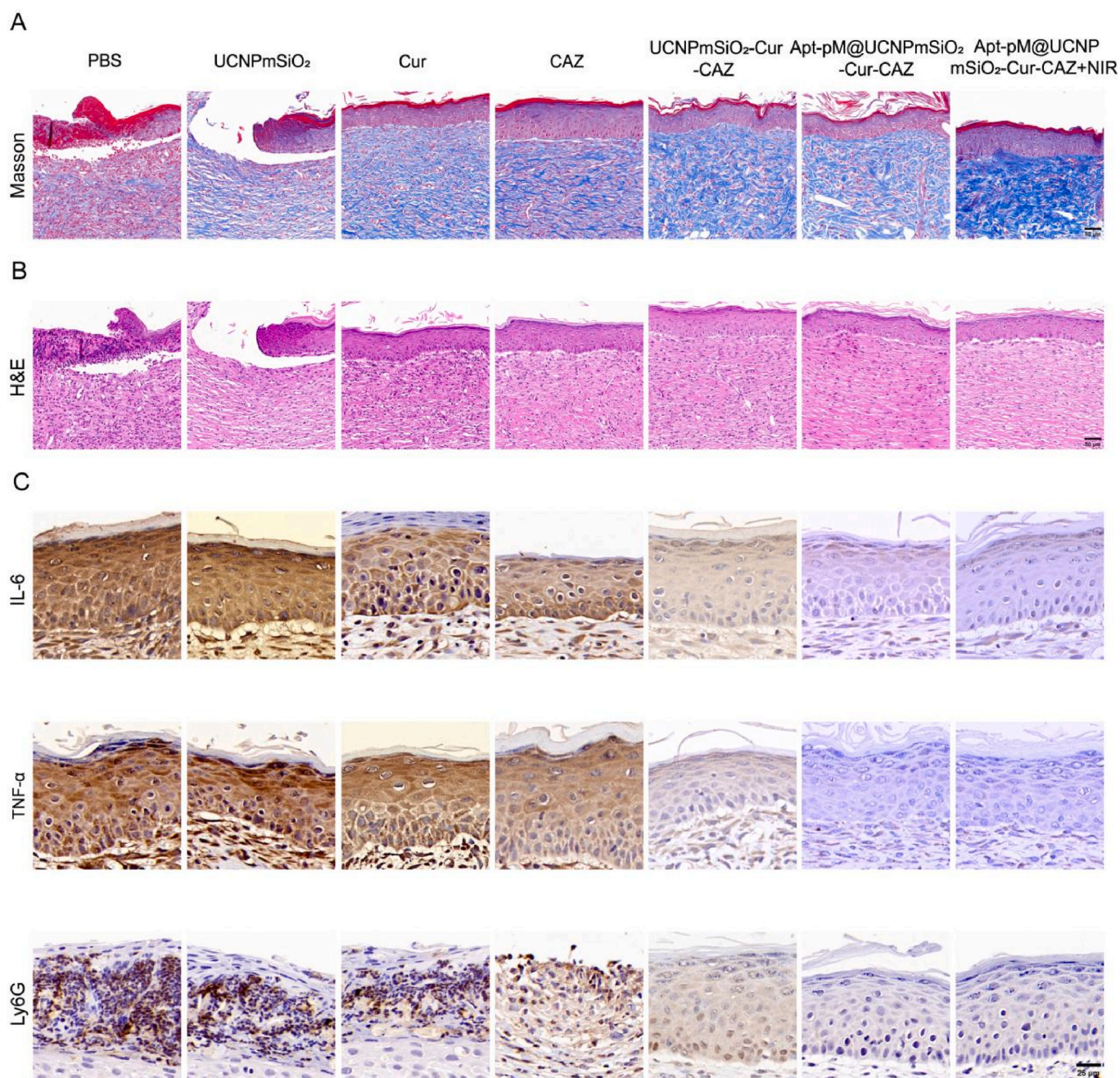


**Fig. 7.** Apt-pM@UCNPmSiO<sub>2</sub>-Cur-CAZ facilitates skin tissue regeneration. (A) Masson staining images of skin wounds. Scale bar: 50  $\mu$ m. (B) H&E staining images of skin wounds. Scale bar: 50  $\mu$ m. (C) Immunohistochemical staining of IL-6, TNF- $\alpha$  and Ly6G in skin wounds. Scale bar: 25  $\mu$ m.

through H&E staining. The PBS group showed a significant infiltration of neutrophils and inflammatory cells, while the NIR irradiated Apt-pM@UCNPmSiO<sub>2</sub>-Cur-CAZ group exhibited a lower number of neutrophils and inflammatory cells, similar to that of normal skin tissue (Fig. 7B). The expression of TNF- $\alpha$ , IL-6 and Ly6G in wound tissue was examined by immunohistochemical staining. Positive expression resulted in yellow or brown staining. The positive expression levels of TNF- $\alpha$ , IL-6 and Ly6G were higher in the PBS group, while the expression levels of inflammatory factors were downregulated and returned to normal in the NIR-irradiated Apt-pM@UCNPmSiO<sub>2</sub>-Cur-CAZ group (Fig. 7C). It was shown that the NIR-irradiated Apt-pM@UCNPmSiO<sub>2</sub>-Cur-CAZ group had an anti-inflammatory effect and contributed to the healing of infected wounds.

### 3.6. In vivo toxicity assessment of Apt-pM@UCNPmSiO<sub>2</sub>-Cur-CAZ

In order to test whether the Apt-pM@UCNPmSiO<sub>2</sub>-Cur-CAZ nano-systems can be used in the clinic against *P. aeruginosa*, the paper evaluated the potential toxicity in vivo by injecting the corresponding treated drugs into the tail vein of mice and observing the toxicity monitoring indexes and organ structures on day 12. The body weights of all mice on days 0, 3, 6, 9 and 12 were also recorded and it was found that there were no significant differences in body weights between the six groups (Fig. 8A). In addition, the levels of WBC, RBC, Hb and PLT were determined using whole blood samples and there was no significant difference in the counts between the groups (Fig. 8B). In this study, kidney function indices (BUN, CREA) and liver function indices (ALT, AST) were also determined using mice serum. Compared with the PBS group, the results of each group showed no significant abnormality

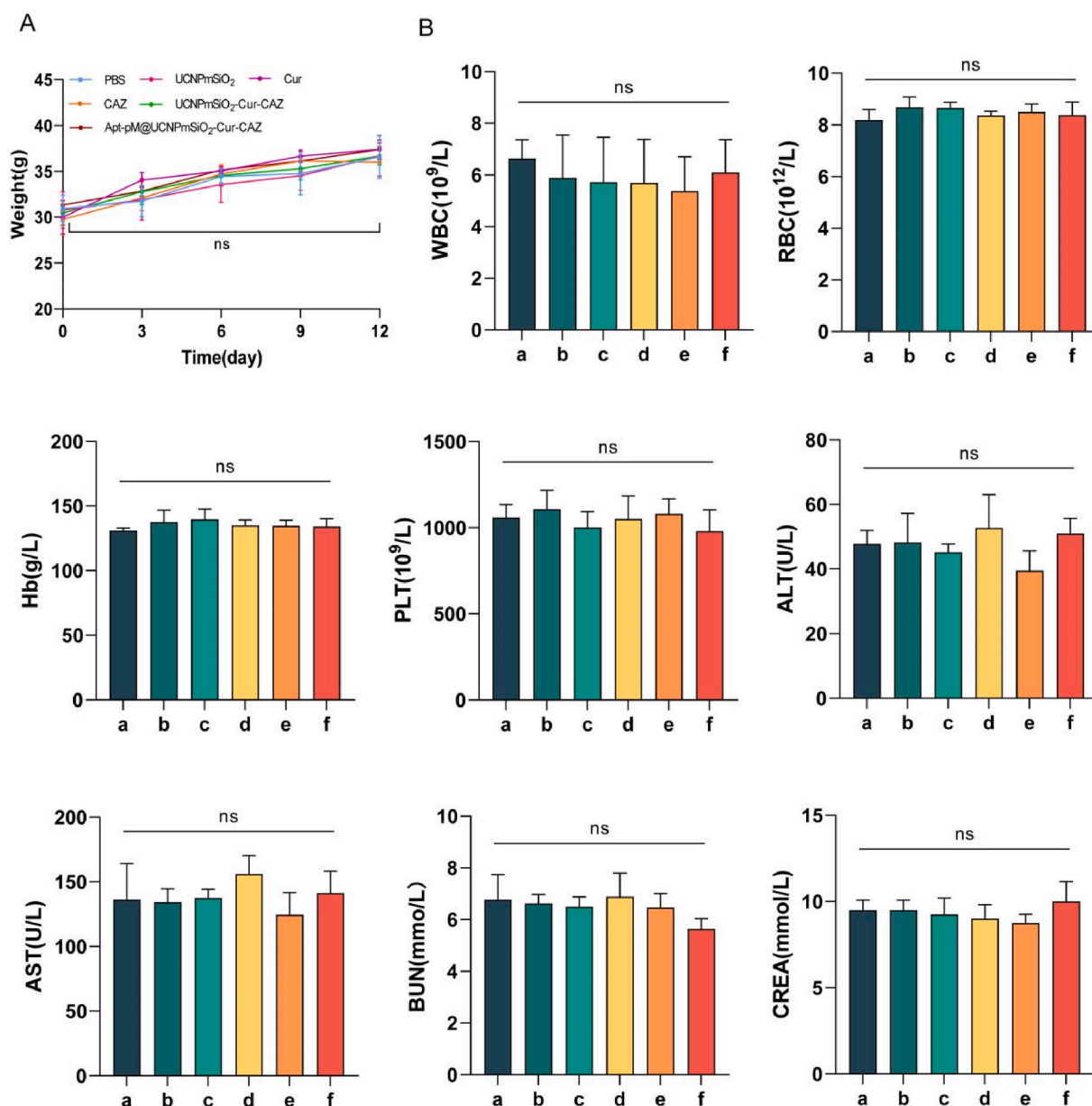


**Fig. 8.** In vivo toxicity assay of Apt-pM@UCNPmSiO<sub>2</sub>-Cur-CAZ. a, PBS; b, UCNPmSiO<sub>2</sub>; c, Cur; d, CAZ; e, UCNPmSiO<sub>2</sub>-Cur-CAZ; f, Apt-pM@UCNPmSiO<sub>2</sub>-Cur-CAZ. (A) Mice weight changes after injecting with different treatments during 12 days. (B) Blood routine examination and serum indexes in mice at 12 days after intravenous injection of corresponding drugs. Data are presented as means  $\pm$  SD (n = 4). ns = no significance.

(Fig. 8B), indicating that Apt-pM@UCNPmSiO<sub>2</sub>-Cur-CAZ had no significant liver and kidney toxicity.

H&E staining facilitates the observation of changes in tissue structure. Therefore, in this study, the toxicity of Apt-pM@UCNPmSiO<sub>2</sub>-Cur-CAZ nanocomposites on major organs (heart, liver, spleen, lung, kidney) was evaluated using H&E staining. As shown in Fig. 9, the UCNPmSiO<sub>2</sub>, Cur, CAZ, UCNPmSiO<sub>2</sub>-Cur-CAZ and Apt-pM@UCNPmSiO<sub>2</sub>-Cur-CAZ groups showed no pathology of inflammatory lesions, fibrosis and necrosis in the heart, liver, spleen, lungs and kidneys compared to the PBS control group. Tissue cells were intact with clear nuclei and no obvious tissue damage was observed. In summary, the Apt-pM@UCNPmSiO<sub>2</sub>-Cur-CAZ nanosystem has good biological safety and no obvious toxic side effects.

#### 4. Conclusion

In this study, Apt-pM@UCNPmSiO<sub>2</sub>-Cur-CAZ was successfully

synthesized and this delivery system exhibited highly efficient antimicrobial activity that was superior to the use of antibiotics alone. In addition, Apt-pM@UCNPmSiO<sub>2</sub>-Cur-CAZ was able to inhibit the formation of *Pseudomonas aeruginosa* biofilms and further remove existing biofilms. Interestingly, the NIR light could enhance the antibacterial and anti-biofilm effects of Apt-pM@UCNPmSiO<sub>2</sub>-Cur-CAZ due to the photodynamic action. Furthermore, Apt-pM@UCNPmSiO<sub>2</sub>-CAZ exploited the high affinity of pre-treated macrophage membranes for LPS and the high targeting properties of nucleic acid aptamers for *Pseudomonas aeruginosa* to bi-directionally target *Pseudomonas aeruginosa* for enhanced antimicrobial efficacy. Moreover, Apt-pM@UCNPmSiO<sub>2</sub>-Cur-CAZ had good haemocompatibility, no significant effect on cell activity and apoptosis, no in vivo toxicity and good biosafety. Apt-pM@UCNPmSiO<sub>2</sub>-Cur-CAZ also promoted the healing of infected wounds and reduced the levels of wound inflammatory factors. The antimicrobial nanosystem with photodynamic therapy is expected to be an effective clinical antimicrobial agent, providing new strategies and

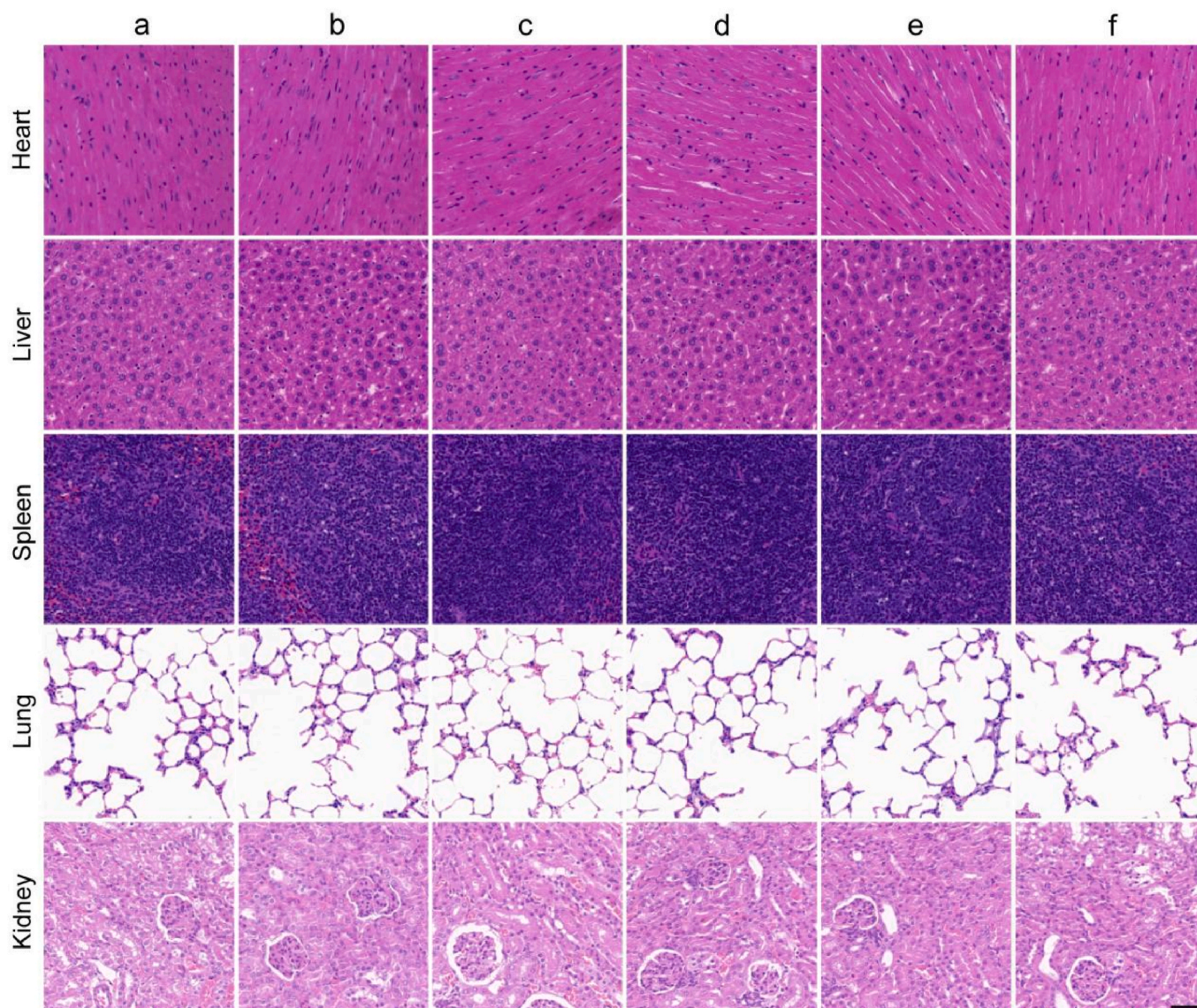


**Fig. 9.** Nontoxic side effects of the Apt-pM@UCNPmSiO<sub>2</sub>-Cur-CAZ in vivo. On the 12 day after respectively injecting with corresponding drugs, the histological evaluation of heart, liver, spleen, lung, and kidney by H&E staining. Scale bar: 50  $\mu$ m.

ideas for the treatment of *Pseudomonas aeruginosa*.

#### CRedit authorship contribution statement

**Chang Ni:** Writing – original draft, Validation, Software, Methodology, Formal analysis, Data curation, Conceptualization. **Xisheng Li:** Formal analysis, Data curation, Investigation, Methodology, Writing – review & editing. **Haiye Jiang:** Software, Investigation. **Shumin Gui:** Investigation. **Heng Yin:** Methodology. **Xinmin Nie:** Writing – review & editing, Supervision, Resources, Project administration, Methodology, Funding acquisition, Conceptualization.

#### Disclosure

The authors declare that they have no known competing interests.

#### Declaration of competing interest

The authors declare that they have no known competing financial interests or personal relationships that could have appeared to influence the work reported in this paper.

#### Acknowledgments

This work was supported by the National Natural Science Foundation of China (Grant No. 81971748); Hunan Provincial Natural Science Foundation of China (Grant No. 2024JJ9044); Key Research and Development Program of Hunan Province (Grant No. 2022SK2004); Science and Technology Program of Changsha (Grant No. kh2201057); Graduate Self-Exploration and Innovation Project of the Central South University of China (Grant no. 2022ZZTS0284, 2024ZZTS0968).

#### Appendix A. Supplementary data

Supplementary data to this article can be found online at <https://doi.org/10.1016/j.mtmbio.2025.101470>.

#### Data availability

Data will be made available on request.

## References

- [1] M. Farahani, A. Shafiee, Wound healing: from passive to smart dressings, *Adv Healthc Mater* 10 (16) (2021) e2100477.
- [2] G.C. Gurtner, S. Werner, Y. Barrandon, et al., Wound repair and regeneration, *Nature* 453 (7193) (2008) 314–321.
- [3] S.A. Eming, P. Martin, M. Tomic-Canic, Wound repair and regeneration: mechanisms, signaling, and translation, *Sci. Transl. Med.* 6 (265) (2014) 265sr6.
- [4] S. Guo, L.A. Dipietro, Factors affecting wound healing, *J. Dent. Res.* 89 (3) (2010) 219–229.
- [5] A. Atala, D.J. Irvine, M. Moses, et al., Wound healing versus regeneration: role of the tissue environment in regenerative medicine, *MRS Bull.* 35 (8) (2010), <https://doi.org/10.1557/mrs2010.528>.
- [6] S.R. Nussbaum, M.J. Carter, C.E. Fife, et al., An economic evaluation of the impact, cost, and medicare policy implications of chronic nonhealing wounds, *Value Health* 21 (1) (2018) 27–32.
- [7] S. Qin, W. Xiao, C. Zhou, et al., *Pseudomonas aeruginosa*: pathogenesis, virulence factors, antibiotic resistance, interaction with host, technology advances and emerging therapeutics, *Signal Transduct Target Ther* 7 (1) (2022) 199.
- [8] K. Poole, *Pseudomonas aeruginosa*: resistance to the max, *Front. Microbiol.* 2 (2011) 65.
- [9] E.B. Breidenstein, C. de la Fuente-Núñez, R.E. Hancock, *Pseudomonas aeruginosa*: all roads lead to resistance, *Trends Microbiol.* 19 (8) (2011) 419–426.
- [10] J.P. Horcajada, M. Montero, A. Oliver, et al., Epidemiology and treatment of multidrug-resistant and extensively drug-resistant *Pseudomonas aeruginosa* infections, *Clin. Microbiol. Rev.* 32 (4) (2019) e00031, 19.
- [11] L.B. Rice, Federal funding for the study of antimicrobial resistance in nosocomial pathogens: no ESKAPE, *J. Infect. Dis.* 197 (8) (2008) 1079–1081.
- [12] Y. Huang, L. Mu, X. Zhao, et al., Bacterial growth-induced tobramycin smart release self-healing hydrogel for *Pseudomonas aeruginosa*-infected burn wound healing, *ACS Nano* 16 (8) (2022) 13022–13036.
- [13] Y. Huang, L. Bai, Y. Yang, et al., Biodegradable gelatin/silver nanoparticle composite cryogel with excellent antibacterial and antibiofilm activity and hemostasis for *Pseudomonas aeruginosa*-infected burn wound healing, *J. Colloid Interface Sci.* 608 (Pt 3) (2022) 2278–2289.
- [14] M. Ruffin, E. Brochiero, Repair process impairment by *Pseudomonas aeruginosa* in epithelial tissues: major features and potential therapeutic avenues, *Front. Cell. Infect. Microbiol.* 9 (2019) 182.
- [15] S.S. Garg, R. Dubey, S. Sharma, et al., Biological macromolecules-based nanoformulation in improving wound healing and bacterial biofilm-associated infection: a review, *Int. J. Biol. Macromol.* 247 (2023) 125636.
- [16] Y.K. Wu, N.C. Cheng, C.M. Cheng, Biofilms in chronic wounds: pathogenesis and diagnosis, *Trends Biotechnol.* 37 (5) (2019) 505–517.
- [17] P. Kolimi, S. Narala, D. Nyavanandi, et al., Innovative treatment strategies to accelerate wound healing: trajectory and recent advancements, *Cells* 11 (15) (2022) 2439.
- [18] W. Liu, Y. Zhang, W. You, et al., Near-infrared-excited upconversion photodynamic therapy of extensively drug-resistant *Acinetobacter baumannii* based on lanthanide nanoparticles, *Nanoscale* 12 (26) (2020) 13948–13957.
- [19] Y. Wang, Y. Yang, Y. Shi, et al., Antibiotic-free antibacterial strategies enabled by nanomaterials: progress and perspectives, *Adv Mater* 32 (18) (2020) e1904106.
- [20] M.A. Mofazzal Jahromi, P. Sahandi Zangabad, S.M. Moosavi Basri, et al., Nanomedicine and advanced technologies for burns: preventing infection and facilitating wound healing, *Adv. Drug Deliv. Rev.* 123 (2018) 33–64.
- [21] K. Malhotra, D. Hrovat, B. Kumar, et al., Lanthanide-doped upconversion nanoparticles: exploring A treasure trove of NIR-mediated emerging applications, *ACS Appl. Mater. Interfaces* 15 (2) (2023) 2499–2528.
- [22] Y. Zhang, P. Huang, D. Wang, et al., Near-infrared-triggered antibacterial and antifungal photodynamic therapy based on lanthanide-doped upconversion nanoparticles, *Nanoscale* 10 (33) (2018) 15485–15495.
- [23] S. Porrang, S. Davaran, N. Rahemi, et al., How advancing are mesoporous silica nanoparticles? A comprehensive review of the literature, *Int J Nanomedicine* 17 (2022) 1803–1827.
- [24] F. Tang, L. Li, D. Chen, Mesoporous silica nanoparticles: synthesis, biocompatibility and drug delivery, *Adv Mater* 24 (12) (2012) 1504–1534.
- [25] W. Wei, Y. Zhang, R. Li, et al., Oral delivery of pterostilbene by L-arginine-mediated "Nano-Bomb" carrier for the treatment of ulcerative colitis, *Int J Nanomedicine* 17 (2022) 603–616.
- [26] Y. Chen, Y. Lu, R.J. Lee, et al., Nano encapsulated curcumin: and its potential for biomedical applications, *Int J Nanomedicine* 15 (2020) 3099–3120.
- [27] K. Zhou, C. Li, D. Chen, et al., A review on nanosystems as an effective approach against infections of *Staphylococcus aureus*, *Int J Nanomedicine* 13 (2018) 7333–7347.
- [28] M.M. Cerveira, H.S. Vianna, E.M.K. Ferrer, et al., Bioprospection of novel synthetic monocurcuminoids: antioxidant, antimicrobial, and in vitro cytotoxic activities, *Biomed. Pharmacother.* 133 (2021) 111052.
- [29] M. Ghasemi, K. Khorsandi, Z. Kianmehr, Photodynamic inactivation with curcumin and silver nanoparticles hinders *Pseudomonas aeruginosa* planktonic and biofilm formation: evaluation of glutathione peroxidase activity and ROS production, *World J. Microbiol. Biotechnol.* 37 (9) (2021) 149.
- [30] I. Ferreira-Faria, S. Yousefial, A. Macário-Soares, et al., Stem cell membrane-coated abiotic nanomaterials for biomedical applications, *J Control Release* 351 (2022) 174–197.
- [31] R.H. Fang, A.V. Kroll, W. Gao, et al., Cell membrane coating nanotechnology, *Adv Mater.* 30 (23) (2018) e1706759.
- [32] B.T. Luk, L. Zhang, Cell membrane-camouflaged nanoparticles for drug delivery, *J Control Release* 220 (Pt B) (2015) 600–607.
- [33] H. Hu, S.Y. Hua, X. Lin, et al., Hybrid biomimetic membrane coated particles-mediated bacterial ferroptosis for acute MRSA pneumonia, *ACS Nano* 17 (12) (2023) 11692–11712.
- [34] R. Huang, G.Q. Cai, J. Li, et al., Platelet membrane-camouflaged silver metal-organic framework drug system against infections caused by methicillin-resistant *Staphylococcus aureus* [published correction appears in *J Nanobiotechnology*. 2021 Sep 19;19(1):278], *J Nanobiotechnology* 19 (1) (2021) 229.
- [35] K.M. Sheu, A. Hoffmann, Functional hallmarks of healthy macrophage responses: their regulatory basis and disease relevance, *Annu. Rev. Immunol.* 40 (2022) 295–321.
- [36] K.A. Fitzgerald, J.C. Kagan, Toll-like receptors and the control of immunity, *Cell* 180 (6) (2020) 1044–1066.
- [37] P.R. Taylor, L. Martinez-Pomares, M. Stacey, et al., Macrophage receptors and immune recognition, *Annu. Rev. Immunol.* 23 (2005) 901–944.
- [38] S. Akira, K. Takeda, T. Kaisho, Toll-like receptors: critical proteins linking innate and acquired immunity, *Nat. Immunol.* 2 (8) (2001) 675–680.
- [39] D.M. Mosser, J.P. Edwards, Exploring the full spectrum of macrophage activation [published correction appears in *Nat Rev Immunol*.2010 Jun;10(6):460], *Nat. Rev. Immunol.* 8 (12) (2008) 958–969.
- [40] C. Wang, Y. Wang, L. Zhang, et al., Pretreated macrophage-membrane-coated gold nanocages for precise drug delivery for treatment of bacterial infections, *Adv Mater.* 30 (46) (2018) e1804023.
- [41] G. Zhu, X. Chen, Aptamer-based targeted therapy, *Adv. Drug Deliv. Rev.* 134 (2018) 65–78.
- [42] J. Soundy, D. Day, Selection of DNA aptamers specific for live *Pseudomonas aeruginosa*, *PLoS One* 12 (9) (2017) e0185385.
- [43] S.H. Khatami, S. Karami, H.R. Siahkouchi, et al., Aptamer-based biosensors for *Pseudomonas aeruginosa* detection, *Mol. Cell. Probes* 66 (2022) 101865.
- [44] X. Zheng, S. Gao, J. Wu, et al., Recent advances in aptamer-based biosensors for detection of *Pseudomonas aeruginosa*, *Front. Microbiol.* 11 (2020) 605229.